Available online at BCREC website: https://bcrec.id

Bulletin of Chemical Reaction Engineering & Catalysis, 18 (2) 2023, 238-255

Research Article

Predicting Photocatalytic Properties of Metal Coupled Mn-TiO_2 Particle Using Response Surface Methodology (RSM) as a Potential Filler in LED's Encapsulant

Amna Jwad Kadem, Yin Xin Teo, Swee-Yong Pung, Srimala Sreekantan, Sivakumar Ramakrishnan*

School of Materials and Mineral Resources Engineering, Engineering Campus, Universiti Sains Malaysia, 14300 Nibong Tebal, Penang, Malaysia.

Received: 21st April 2023; Revised: 29th May 2023; Accepted: 30th May 2023
Available online: 4th June 2023; Published regularly: July 2023

Abstract

This study addresses yellowing discoloration in LEDs caused by TiO_2 particle degradation in encapsulants. The commonly added TiO_2 particles will enhance light reflectance, and accelerate photodegradation but will decrease LED lifespan by lowering lumen quality and causing chromaticity change. To mitigate these effects, Mn particles were coupled with TiO_2 particles using photo-reduction. This research examined three parameters Mn^{2+} ions concentration, UV irradiation duration, and annealing temperature, and the successful Mn-TiO_2 coupling achieved. The resulting Mn-TiO_2 particles, synthesized at 20 ppm Mn^{2+} ions and 200 °C annealing temperature, exhibited superior dispersibility and minimal agglomeration compared to TiO_2 particles. Next, the photocatalytic performance of Mn-TiO_2 particles was optimized using Response Surface Methodology (RSM). These particles exhibited the lowest photodegradation with a rate constant of 0.03092 min^{-1} and achieved a photodegradation efficiency of 79.92% at 60 min, amongst the others. Photodegradation of methylene blue followed a 1st-order kinetic model. Despite a slightly higher refractive index (RI), epoxy thin films with Mn-TiO_2 particles displayed higher transmittance. Mn-TiO_2 particles can thus serve as fillers in LED encapsulants to increase RI, reduce photodegradation, and enhance TiO_2 particle dispersion.

Keywords: LED encapsulant; Mn-TiO_2 particles; Photocatalytic; DOE; RSM; Response Surface Methodology; Design of Experiment

How to Cite: A.J. Kadem, Y.X. Teo, S.-Y. Pung, S. Sreekantan, S. Ramakrishnan (2023). Predicting Photocatalytic Properties of Metal Coupled Mn-TiO_2 Particle Using Response Surface Methodology (RSM) as a Potential Filler in LED's Encapsulant. *Bulletin of Chemical Reaction Engineering & Catalysis*, 18(2), 238-255 (doi: 10.9767/bcrec.18020)

Permalink/DOI: https://doi.org/10.9767/bcrec.18020

1. Introduction

Around 50 years ago, the technology for light-emitting diodes (LEDs) was created [1,2], and they have been regarded as the most promising light sources for the future due to their unique qualities, which include great durability, environmental friendliness, high efficiency, low voltage operation, low power consumption, and high brightness [3–6]. In a typical LED device, a lighting chip and packaging material are the main components that determine the light-emitting efficacy [7]. To compete in the general illumination market, higher light output with a longer life span is required [8]. Most of the LED failures are related to its package as it acts as a cover to protect microelectronic components from direct contact with the aggressive system

* Corresponding Author.
Email: srsivakumar@usm.my (S. Ramakrishnan)

and environmental stresses [9,10]. The packaging material requires a high refractive index (RI), high resistance to chemical attack, strong adhesion and bond strength, high mechanical strength, and stable microstructure [9,11]. Silicon and epoxy are widely used as encapsulant materials in LED applications [12–16]. However, silicone-based encapsulants have low RI which limits the light extraction efficiency.

One of the issues with LED failure is the yellowing chromaticity discoloration caused by the degradation of polymeric materials when exposed to light and elevated temperatures, leading to chemical degradation through mechanisms such as chain scission and oxidation. Yellowing chromaticity discoloration of encapsulants produces an increased absorption of blue light. The photodegradation of polymeric materials causes a reduction in their transparency, and thus, reduces the amount of light emitted. Many efforts were made to solve this problem, such as adding inorganic NPs, to form a composite and synthesizing silicone/epoxy hybrid resins [17,18]. Epoxy resin has also been adopted as a filling material in typical LEDs, due to mechanical stabilities, moisture resistance, and low price [19–21]. There are several ways to increase the RI of an epoxy encapsulant, such as curing with a cationic initiator, the inclusion of thiol compounds, and TiO_2 or ZrO_2 nanocrystals [22].

Most of the industry practices adding TiO_2 particles into epoxy encapsulant to improve the reflectance of light and thus improves its light extraction efficacy in LEDs. Metal oxides have found many applications in optical, acoustic, luminescent, electronic, and optoelectronic fields. Among such materials, titanium dioxide TiO_2 was chosen due to its size in nanometres, crystallite type as well as physical and chemical properties. According to Alkallas *et al*. [23], the rutile phase is the most thermodynamically stable phase with the highest reflectivity to near-infrared radiation (NIR). This property was suitable to make the white pigments in paints due to the effective light scattering property of such phase structure. However, for LED application, TiO_2 was exposed to UV for a long duration, thus it needs to have high stability. High RI nanoparticles, such as titania TiO_2 nanoparticles, that are dispersed uniformly in an encapsulant, will increase the overall RI of the encapsulant to prevent the photodegradation of polymeric materials [24]. Nevertheless, the presence of TiO_2 particles under blue/UV light irradiation will accelerate the photodegradation of epoxy, causing yellowing chromaticity discoloration of encapsulant and reduction of LED luminance. The yellowing chromaticity discoloration causes the refractive index (RI) mismatches between the lighting chip and encapsulant leading to severe light reflection at the interface of the LED chip and encapsulant, and thus greatly reduces the light emitting efficacy [7]. Therefore, modification of TiO_2 is necessary to improve the stability of TiO_2 against UV irradiation. Constructing heterojunctions can improve the charge carrier's separation, optical absorption, and stability of TiO_2 [25]. Coupling TiO_2 with Mn increased the free radical scavenging ability and make Mn-TiO_2 particles to be potential fillers in LEDs' encapsulation [26]. According to Pinton and S Bulhões, Mn ions lower the photocatalytic activity of the TiO_2 particles in the photodegradation of Rhodamine 6G. This is because Mn ions in the TiO_2 crystalline network act as recombination sites that increase the recombination of photogenerated electron-hole pairs and thus, reducing the photocatalytic activity [27]. In this research, Mn was coupled onto TiO_2 particles to reduce the photodegradation and improve the stability of TiO_2 particles, and Response Surface Methodology (RSM) was used to analyze the impact of process parameters and optimization conditions. The annealing temperature, UV irradiation duration, and metal ion concentration were the variables used in the RSM, based on the design of experiments (DOE).

As photocatalytic performance depends on many factors, it is difficult to solve the photodegradation problem that requires fast coverage testing. Previously, the common one-factor-at-a-time (OFAT) method is used. This method is most used when process factors are independent or rare [28]. Nevertheless, this univariate approach does not present the effects of the interactions among the factors of the process. RSM, based on the DOE is a set of statistical and mathematical tools used for designing the experiments and optimizing the effect of process variables [29]. RSM can evaluate the interactions between testing variables but also minimize the number of experiments to be undertaken [30]. Therefore, the trend was shown toward replacing inefficient practice with effective chemometric methods, including RSM and DOEs [28]. This experimental strategy for seeking the optimum conditions is an efficient technique for use with a multivariable system [31]. According to Song *et al*., RSM has been proven to be a powerful statistical technique for optimizing photocatalytic purification processes and evaluating the interactions of mutually influencing parameters [30].

Various materials have been explored as fillers in LED encapsulants in previous research. However, no studies have investigated the use of Mn-TiO_2 particles to the best of our knowledge. The present work demonstrates, for the first time, that Mn-TiO_2 particles can improve the refractive index, lower photodegradation, and improve the dispersion of TiO_2 particles in an epoxy encapsulant when used as a filler in LED encapsulants. Additionally, the photocatalytic performance of Mn-TiO_2 particles was locally optimized using RSM. An optimized photocatalytic performance was achieved with a rate constant of 0.031 $ppm^{-1}.min^{-1}$ and 79.914% photodegradation efficiency at 60 mins by using 20 ppm of Mn^{2+} ion concentration and annealing the particles at 200 ºC with UV irradiation.

Results demonstrate that the transmittance of epoxy thin films incorporated with Mn-TiO_2 particles was higher than that with TiO_2 particles, highlighting the potential of Mn-TiO_2 as a promising filler in LED. In summary, this work presents a novel approach to improving the performance of LED encapsulants and underscores the potential of Mn-TiO_2 particles in this application.

2. Materials and Methods

2.1. Materials

TiO_2 particles were purchased from Merck and used to couple with manganese acetate ($Mn(CH_3COO)_2.4H_2O$) which was provided by Fluka. MB was used to test its photodegradation. Deionized water was used as a solution during mixing, while distilled water was used to dilute methylene blue.

2.2. Preparative Procedure

0.2230 g of manganese acetate was mixed with 1000 mL of deionized water to obtain a 50 ppm metal solution. The mixture was then stirred for about 2 h. In a typical photoreduction process, 500 mL manganese acetate solution was stirred with 0.50 g TiO_2 in a dark condition for 30 min. Next, the solution was stirred under UV radiation (λ = 100-400 nm) for 1 h. The particles were collected using the centrifuge method and dried overnight at 90 ºC. The steps were repeated for various concentrations of metal ions solutions and durations of UV irradiation. Mn-TiO_2 particles were annealed in a tube furnace. Annealing was carried out to reduce metal oxide to metal and for TiO_2 phase transition purposes. The particles were heated to 500 ºC by 10 ºC/min in an inert atmosphere with nitrogen gas. After that, the particles were soaked for 2 h in a reducing atmosphere with forming gas which contained 5% of hydrogen (H_2) and 95% of nitrogen (N_2). After 2 h, the powder was cooled to room temperature in the inert atmosphere with nitrogen gas again. The steps for annealing were repeated for samples with various concentrations and durations of UV irradiation at different annealing temperatures.

The data sampling plan was based on factorial design 2^3, as shown in Table 1, and additional 3 samples at optimum parameters (50 ppm concentration of Mn^{2+}, 1 h UV irradiation, 500 °C annealing temperature) for model verification. The total number of samples was 11. After collecting all the data, the results were optimized using Response Surface Methodology (RSM) to obtain the lowest photocatalytic activity and the highest reflectance. When the optimum parameters were obtained, the Mn-TiO_2 particles were synthesized using the optimum parameters following the steps discussed above. Subsequently, Mn-TiO_2 particles were incorporated into epoxy resin to observe improvements in three aspects: photodegradation rate, yellowing chromaticity discoloration rate, and refractive index, compared to pure epoxy resin and epoxy resin incorporated with TiO_2 particles.

2.3. Characterization

2.3.1. Structural and morphological

The morphology and structure of the TiO_2 particles and Mn-TiO_2 particles were examined by the field-emission scanning electron microscope (FESEM Gemini Zeiss Supra 35VP), X-Ray Diffraction (XRD Bruker D8 diffractometer), and Energy Dispersive X-Ray spectrophotometer (EDX) that couples with FESEM to analyze the sample's elemental composition.

Table 1. Raw materials used for this project.

Concentration of Mn^{2+} (ppm)	Duration of UV irradiation (h)			
	0		2	
	300 °C	800 °C	300 °C	800 °C
20	a	b	c	d
80	e	f	g	h

2.3.2. Optical properties

Ellipsometer (Sentech SE400 Adv) was used to measure the refractive index (RI). A beam of light with a known polarization state is transmitted or reflected from the surface of the thin film, resulting in a change in its polarization state. The modified polarization state can be decomposed into the reflection coefficients, r_p and r_s. Ellipsometer measures the ratio of r_p and r_s and utilizes this ratio to obtain the ellipsometric angles Δ and ψ as shown in Equation (1). With the measurement of Δ and ψ, a layer model is established for the thin film, which consists of any known optical constants (n, k) and thicknesses (d) of all individual sequential layers within the thin film. Using an iterative approach, the unknown optical constants and thicknesses are then varied until the best match for the measured values of Δ and ψ is obtained [32].

$$\rho = \frac{r_p}{r_s} = \tan\Psi \times e^{i\Delta} \quad (1)$$

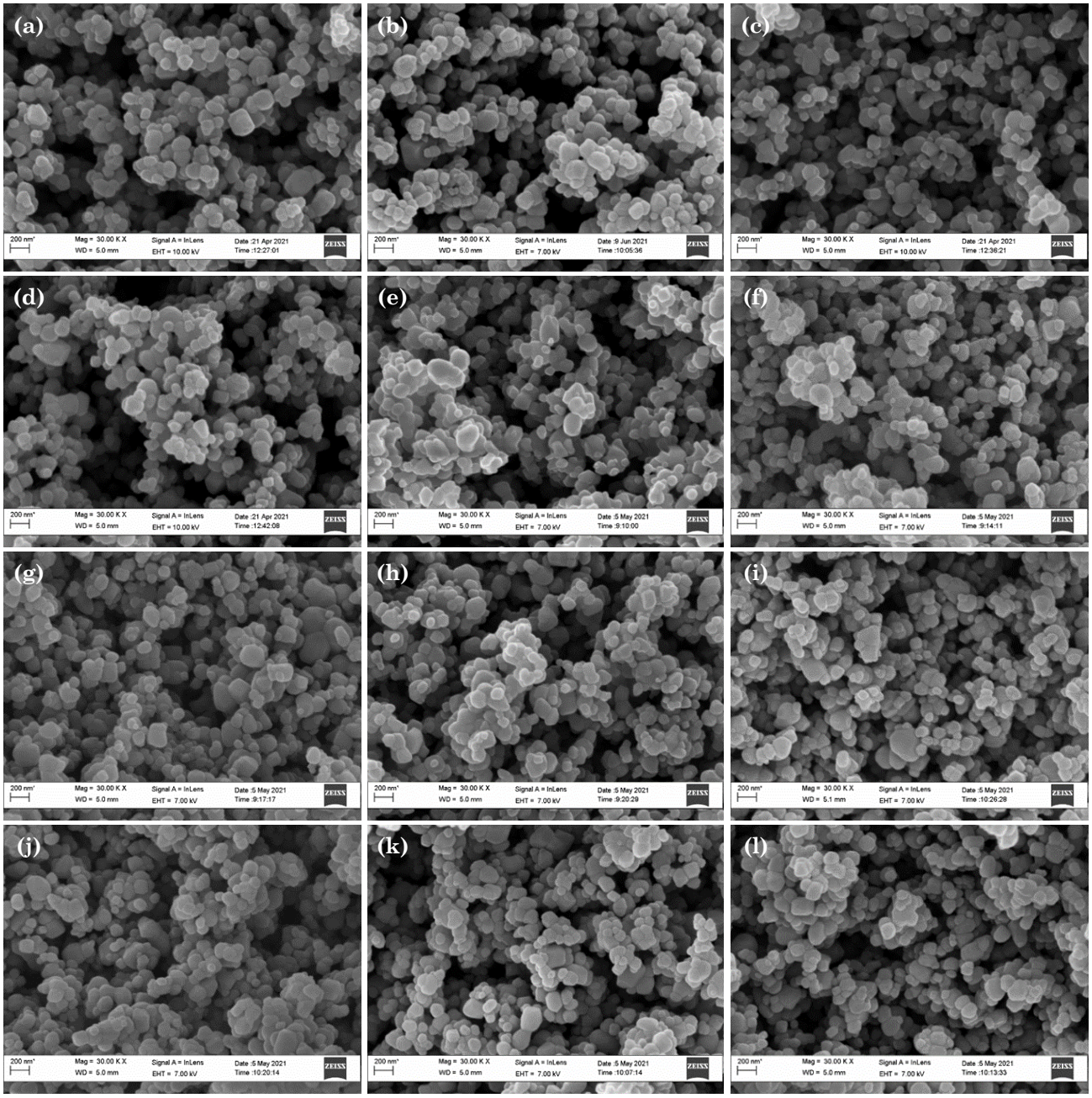

Figure 1. FESEM images (a) TiO_2 particles before and (b) after annealing, (c) $MnTiO_2$ before annealing, (d) Mn-TiO_2 particles 50 ppm, 1 h, 500 °C, (e) 20 ppm, 0 h, 200 °C, (f) 20 ppm, 0 h, 800 °C, (g) 20 ppm, 2 h, 200 °C, (h) 20 ppm, 2 h, 800 °C, (i) 80 ppm, 0 h, 200 °C, (j) 80 ppm, 0 h, 800 °C, (k) 80 ppm, 2 h, 200 °C, (l) 80 ppm, 2 h, 800 °C.

2.3.3. Photocatalytic properties

To study photocatalytic degradation, methylene blue (MB) was chosen. The initial concentration of MB (C_0) was prepared as 5 ppm. 25 mg of Mn-TiO_2 particles prepared under different conditions were weighed and put in a beaker with 250 mL of MB solution. The solutions were stirred in the dark for 30 min followed by 1 h of UV irradiation. Then, it was collected every 15 min. A spectrophotometer (UV-Visible Varian Cary 50) was used to measure the absorbance (A_0) with a wavelength range of 200 to 800 nm. The initial concentration of MB (C_0) was prepared as 5 ppm. The concentration of MB in suspension was analyzed using its characteristic wavelength of maximum absorbance at 664 nm [33]. The photodegradation efficiency was calculated using Equation (3). Langmuir–Hinshelwood expression that explains the kinetics of heterogeneous catalytic systems is given by Equation (4), Then when Equation (4) was integrated, we get Equations (5) and (6),

$$A_0 = \log_{10}\left(I_0 / I\right) \tag{2}$$

$$\text{Photodegradation efficiency (\%)} = \frac{[C]_0 - [C]}{[C]_0} \times 100 = \frac{A_0 - A_t}{A_0} \times 100 \tag{3}$$

$$r = -\frac{dC}{dt} = \frac{k_t K[C]}{1 + K[C]} \tag{4}$$

$$[C] = [C]_0 e^{-k_{app} \times t} \tag{5}$$

$$\ln\left(\frac{[C]}{[C]_0}\right) = -k_{app} \times t \tag{6}$$

where, $[C]_0$ and $[C]$ are the original and residual MB dye concentrations respectively, A_0 and A_t the absorbance of MB before and after UV irradiation at t time, r was the rate of dye mineralization, k_t was the rate constant, and K was the adsorption coefficient. k_{app} (k_tK at Equation (4)) was the apparent reaction rate constant (min^{-1}), and $[C]_t$ was the concentration of MB at each time [34].

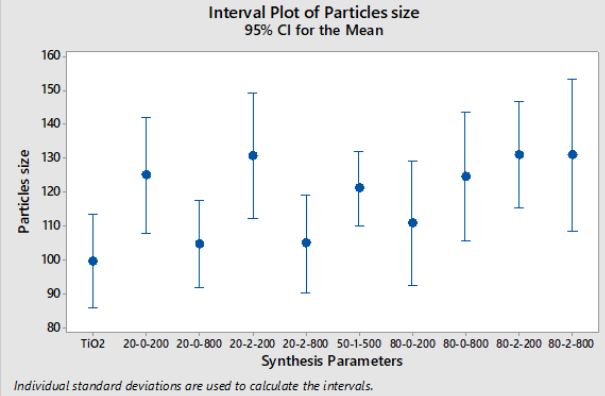

Figure 2. Particle size of Mn-TiO_2 synthesized at various parameters.

2.4. Zeta potentials

Zeta potentials were measured using (Malvern zeta sizer ZS90) with a dispersion of 0.5 mg Mn-TiO_2 particles in 55 mL of deionized water. The solution was then sonicated at 25 °C for 30 min. The stability limit of particles was determined by the zeta potential (ζ). This stability is achieved due to electrostatic repulsion between particles adsorbed on the surface of TiO_2, which prevents them from agglomerating [27]. A large value of zeta potential indicates good physical stability. A small zeta potential value can result in physical instability due to particle aggregation and flocculation due to the van der Waals attractive forces [35].

2.5. DOE and RSM

The synthesis parameters, *i.e.* concentration of metal ion solution, duration of UV irradiation and annealing temperature were varied to synthesize the Mn-TiO_2 particles to have a higher reflectance but a lower photocatalytic activity to be used as filler in the LED encapsulant. The result for reflectance and photocatalytic properties were then collected and analysed using Design of Experiments and Response Surface Methodology in Minitab 18 statistical software. The sampling was based on 2^{3-1}+3 factorial design.

3. Results and Discussion

3.1. Structural and Morphological Analyses

Figure 1(a)-(b) shows the morphology of TiO_2 particles before and after annealing at 500 °C for 2 h respectively. The TiO_2 particles were spherical in shape, and there was not much difference in the morphology of TiO_2 particles before and after annealing. The average particle sizes for TiO_2 before and after annealing were 99.8±36.9 nm and 91.4±34.5 nm, respectively, as measured using a software analyser (ImageJ) (sample size of 30). From the two-sample t-test result (α = 0.05), there was no significant difference in size between TiO_2 particles before and after annealing. No obvious difference in morphology after the deposition of Mn as shown in Figure 1(c). The Mn-TiO_2 particles made with different Mn concen-

trations and UV irradiation periods are shown in Figure 1(d)-(l).

The average particle size of Mn-TiO_2 as determined by ImageJ is shown in Figure 2. The Mn-TiO_2 was larger than TiO_2 particles, this was due to the metal deposited on the TiO_2 surface which led to the increment of total particle size. In addition, the size of the Mn-TiO_2 particles before annealing is greater than after annealing, suggesting that the annealing removed some of the hydrocarbons from the Mn deposits on the surface of TiO_2 particles, as the precursor used for deposition was manganese acetate [$Mn(CH_3COO)_2.4H_2O$], and thus reduced the particles size after the annealing. The size of Mn-TiO_2 particles with 80 ppm Mn^{2+}, 2 h UV irradiation time and 200 °C annealing temperature was the largest (131.1±42.1 nm) whereas the particles size of Mn-TiO_2 with 20 ppm Mn^{2+} that did not undergo UV irradiation but anneal at 800 °C was the smallest (104.9±34.8 nm) when compared to other Mn-TiO_2 particles that synthesized in various conditions. A higher Mn^{2+} ions concentration resulted in larger particle size as more Mn^{2+} ions could be deposited on the TiO_2 particles. UV irradiation initiated photoreduction of the Mn^{2+} ions to Mn particles, and annealing at a higher temperature in the reductive environment (5% H_2 and 95% of N_2) was able to reduce more oxide from MnO_2. This reduced the particle size as well.

EDX was carried out on the TiO_2 and Mn-TiO_2 particles before and after annealing for elemental analysis as shown in Figure 3. The atomic percentages of Ti and O before annealing were 33.44% and 66.56%, with a ratio close to 1:2. Nevertheless, the atomic percentage of Ti increased to 38.8 at% while the atomic percentage of O decreased to 61.2 at% after being annealed at 500 °C for 2 h in the reductive environment (5% H_2 and 95% N_2). The atomic ratio changed to around 1:1.6 after annealing. This result indicates that annealing in the reductive environment using forming gas was effective to remove oxygen from MnO_2 particles and TiO_2 particles (side effect) to produce Mn-TiO_2 particles. The hydrogen gas (from forming gas) could react with oxygen from the metal oxides and was removed as water during the annealing. The removal of O atoms from the TiO_2 particles left two excess electrons on the empty states of Ti cations. The electrons could be either localized or distributed among the 5-fold coordinated Ti^{3+} ions surrounding the O vacancy [35]. This led to a partial reduction of Ti (IV) ions. The EDX results had proven the presence of Mn deposited on TiO_2 particles.

The XRD patterns of TiO_2 and Mn-TiO_2 at different synthesis parameters are illustrated in Figure 4(a)-(c) The XRD patterns of TiO_2 and Mn-TiO_2 at different synthesis parameters. The diffraction patterns show the pres-

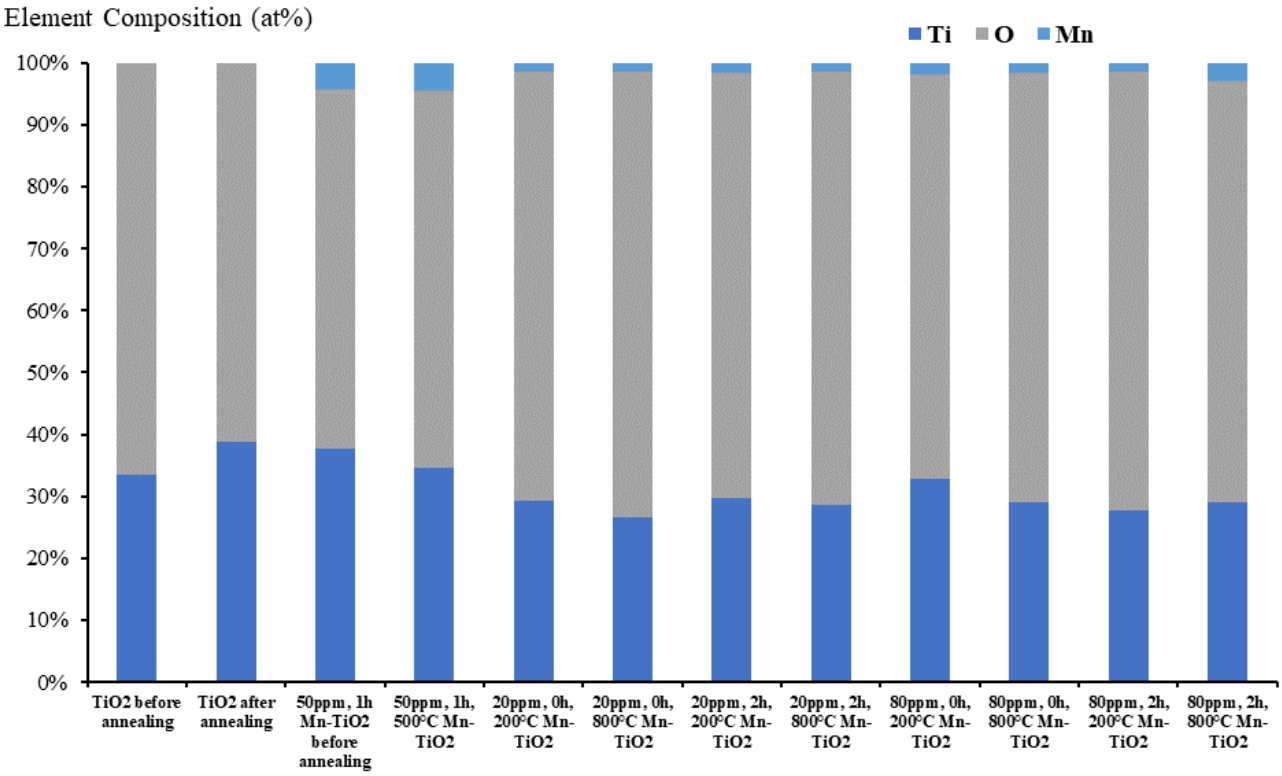

Figure 3. EDX analysis of Mn-TiO_2 particles synthesized under different parameters.

ence of TiO_2 (ICSD 98-007-6028) as anatase at 500 °C, anatase and brookite at 200 °C, and anatase and rutile at 800 °C. This indicates the occurrence of phase transformation at different annealing temperatures. The sharp peaks indicated that the samples were in a crystalline structure. All these three annealing temperatures have diffraction peaks at 25.3°, 37.8°, 48.1°, 53.9°, 55.1°, 62.7°, 68.8°, 70.3°, 75.1°, and 82.7° correspond to (011), (004), (020), (015), (121), (024), (116), (220), (125), and (224) respectively for anatase. The XRD results show that anatase was still dominant in both TiO_2 and Mn-TiO_2 particles. There was no diffraction peak corresponding to Mn except the one synthesis at 200 °C. This may be due to the amount of Mn present being below the detection limit of XRD [36]. Hence, in this work, it can be explained that the absence of additional peaks was due to the trace amount of Mn deposited on TiO_2 particles as EDX results already showed that the atomic percentage of Mn-TiO_2 particles did not exceed 5%.

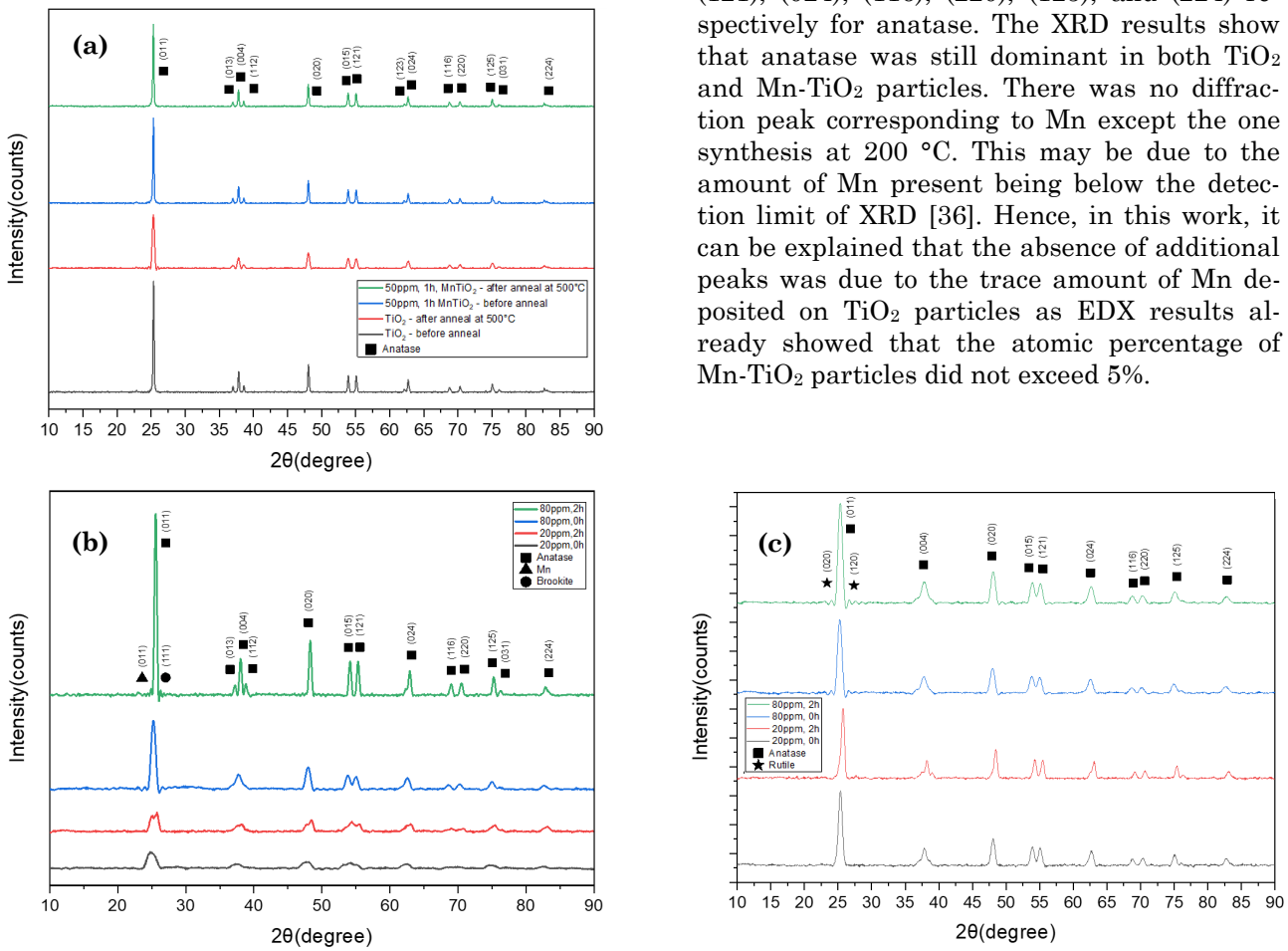

Figure 4. XRD pattern for (a) TiO_2 and Mn-TiO_2 particles before and after annealing at 500 °C, (b) Mn-TiO_2 particles annealing at 200 °C (c) Mn-TiO_2 particles annealing at 800 °C.

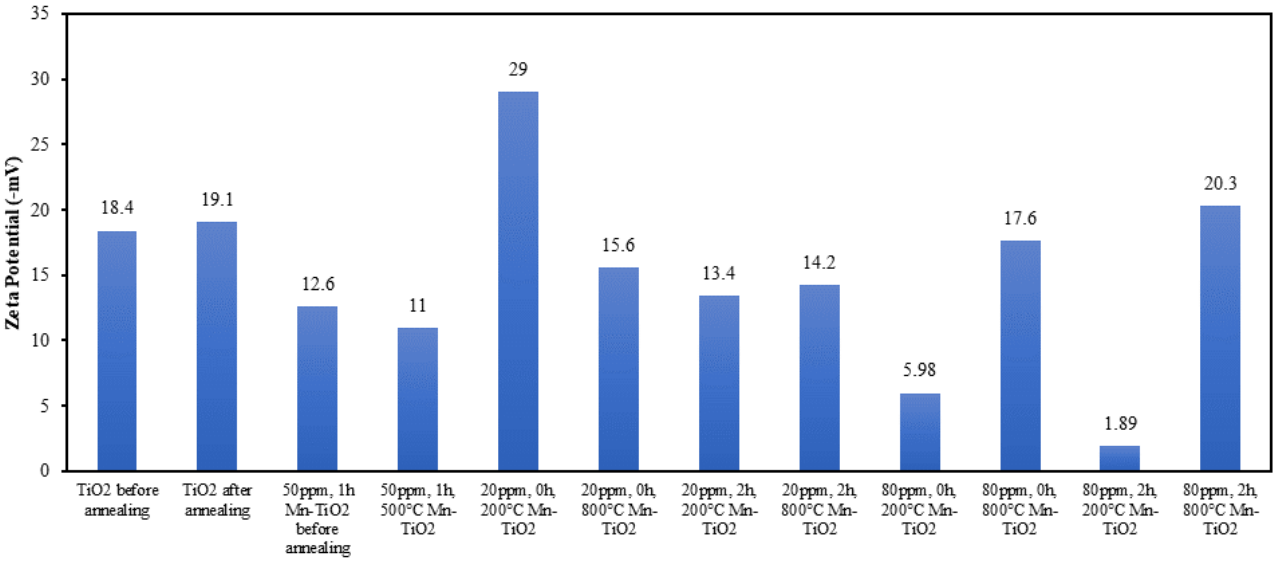

Figure 5. Zeta potential of TiO_2 particles and Mn-TiO_2 particles.

3.2. Zeta Potential Analysis

Figure 5 shows the zeta potential of all patterns. The zeta potential varied between −30mV to +30mV which means that all the samples were not stable. Thus, the particles tend to agglomerate as observed in FESEM images. Mn-TiO_2 particles synthesized using 20 ppm Mn^{2+} ions, 200 °C annealing temperature without UV irradiation show the highest zeta potential value. Thus, it is the most stable particle in solution as compared to others. It has a lower tendency to agglomerate compared to pure TiO_2 particles. Besides, zeta potential shows the surface of TiO_2 particles and Mn-TiO_2 particles were negatively charged, and hence the positively charged organic dye, *i.e.*, MB, was able to adsorb on the surface of the photocatalyst for the photodegradation process.

3.3. Photocatalytic Properties

Photocatalytic performances of TiO_2 particles and Mn-TiO_2 particles (synthesis condition: 20 ppm Mn^{2+}, 200 °C) were evaluated through photodegradation of MB. From the UV-Vis result obtained in Figure 6(a)-(b), the characteristic absorption peak of MB was centred at 663 nm with a shoulder at 615 nm. The observed absorption peak at 663 nm corresponds to the transitions between the ground state (S) and the first excited singlet state (SI) of the dye molecules when the sample was irradiated with photon energy. The absorption peak of the spectra rapidly decreased with increased time and almost disappeared for 60 min light irradiation due to N-demethylation and deamination of MB [37,38]. The degradation of MB indicated that TiO_2 and $MnTiO_2$ in the experiment have photocatalytic activity [39]. The linear fittings (r^2 = 0.98587 and 0.96748) in Figure 6(c) indicate that the photodegradation of MB by TiO_2 particles and Mn-TiO_2 particles followed first-order kinetic under UV-light irradiation. The rate constant, which is determined from the slopes of the plots, are 0.04423 min^{-1} and 0.03092 min^{-1}, respectively. As shown in Figure 6(d), TiO_2 particles recorded a photodegradation efficiency of 90.53% whereas Mn-TiO_2 particles achieved 79.92% at 60 min.

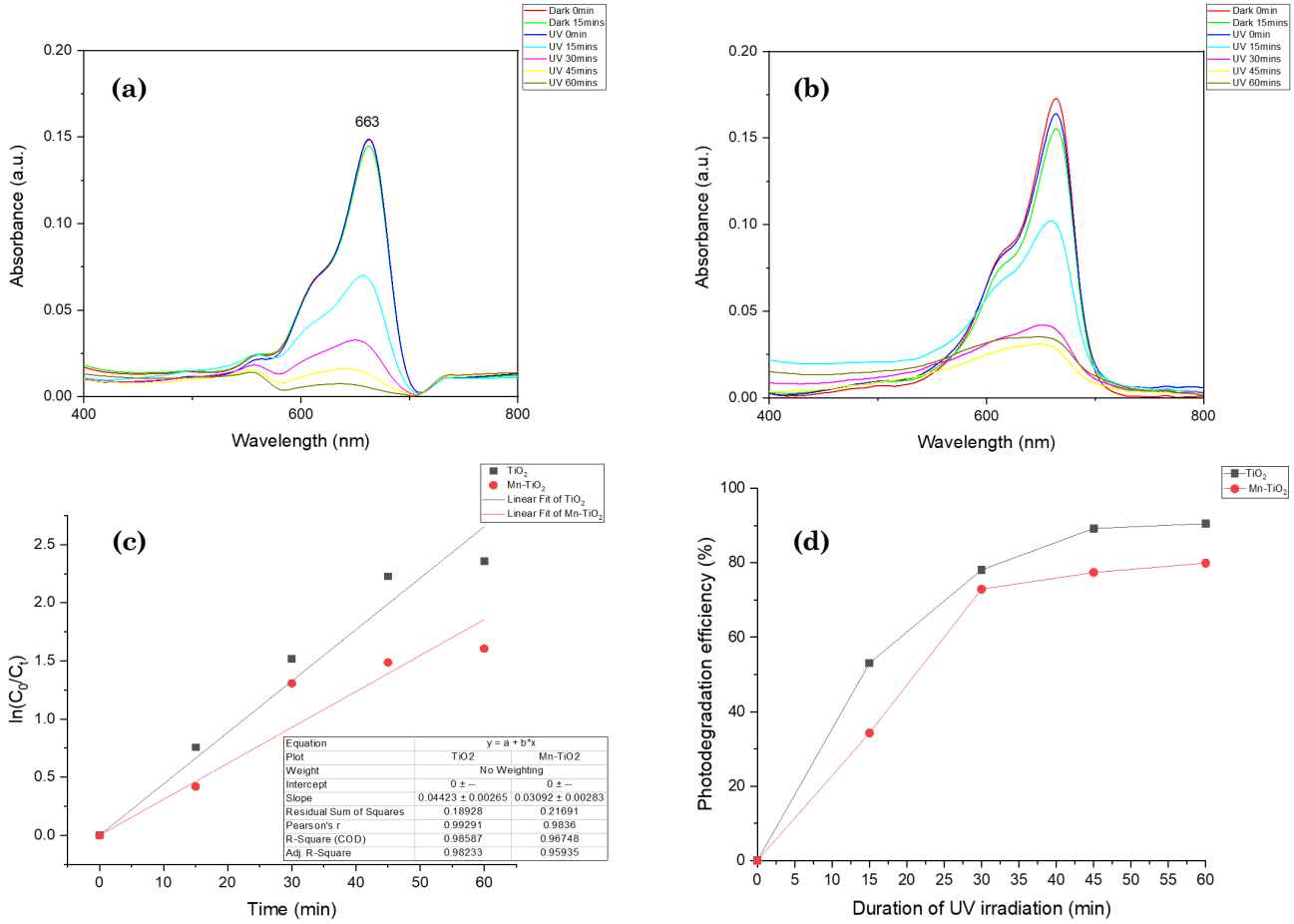

Figure 6. (a) UV-Vis spectra of MB degraded by TiO_2 particles, (b) UV-Vis spectra of MB degraded by Mn-TiO_2 particles (synthesis condition: 20 ppm Mn^{2+} ions, 200 °C annealing temperature), (c) rate constant and (d) photodegradation efficiencies under UV irradiation.

3.4. DOE and RSM Analysis

By using Minitab 18 statistical software, Design of Experiments (DOE) and Response Surface Methodology (RSM) were employed to optimize the synthesis parameters to get the lowest photocatalytic activity of Mn-TiO_2 particles. The details of the experimental parameters are shown in Table 2. The experimental data obtained using the full factorial 2^3 and 3 centre point data sampling plan are displayed in Table 3. The responses were rate constant (RC) and photodegradation efficiency (PE) at 60 mins UV irradiation, and a total of 11 experiment runs were performed. The centre point parameters were decided according to the previous researcher [26].

Table S1 shows the ANOVA results for rate constant (RC). The p values of all factors are more than α (0.05), which indicates the model is not significant. Table S2 displays the RSM results after removing factors AC and ABC because they were not significant. From the Table, we can see the difference between the predicted R-squared (0.7300) and adjusted R-squared (0.8541) is less than 0.12. Similarly, the difference between the R-squared of (0.9352) to the Adjusted R-squared of 0.8541 is very much smaller which is 0.08, and is showing the success of the project. It has been found the interaction of factors BC was found to be the major effect on the RC in comparison to other factors, due to the high F value of (20.19). The individual factor of UV irradiation duration has been found to have less significant effects on RC compared to Mn^{2+} ions concentration and annealing temperature. The presence of curvature could be clearly seen in the 3D surface plot as seen in Figure 7(a) indicating the combined effect of concentration (A) and duration (B) on RC at constant temperature (500 °C). The RC changes due to the influence of concentration and duration at a constant temperature. The minimum RC of 0.0303 $ppm^{-1}min^{-1}$ was obtained. The combined effect of duration (B) and temperature (C) on RC at a constant concentration (50 ppm) was shown in Figure 7(b), the minimum RC has been found to be (0.0308 min^{-1}) by the effect of concentration and time at a stable temperature. The interaction between the duration and temperature was the most effective parameter for minimizing RC in photocatalytic activity. The contour plot in Figure 7(c)-(d) shows that when the temperature is fixed at 500 °C, the concentration and duration need to be maximized to achieve low RC. When concentration is kept at 50 ppm, temperature and duration need to be lower to reduce RC.

Table S3 shows the ANOVA results for photodegradation efficiency (PE), The p-values of all factors are larger than 0.05, indicating that there are no significant terms in this model.

Table 2. Variable parameters of DOE.

Parameters	Unit	Details		
		Minimum	Middle	Maximum
Concentration of Mn^{2+}, A	ppm	20	50	80
UV irradiation periods, B	h	0	1	2
Annealing Temperature, C	°C	200	500	800

Table 3. Mn-TiO_2 particles synthesized using various conditions and their rate constant and photodegradation efficiency.

Concentration of Mn^{2+}, A (ppm)	UV irradiation periods, B (h)	Annealing Temperature, C (°C)	Rate constant, RC ($ppm^{-1}.min^{-1}$)	Photodegradation efficiency at 60 min, PE (%)
20	0	200	0.03092	79.92032
20	0	800	0.04542	90.48597
20	2	200	0.04307	90.51431
20	2	800	0.04010	86.90945
80	0	200	0.03075	84.98312
80	0	800	0.04501	91.30372
80	2	200	0.02995	82.09509
80	2	800	0.03062	83.92060
50	1	500	0.03558	84.60321
50	1	500	0.03163	85.64238
50	1	500	0.03798	88.26125

Model reduction is needed to improve the analysis. Table S4 displays the RSM results after removing the curvature terms because they were not significant. The predicted R-squared of 0.8990 is in reasonable agreement with the adjusted R-squared of 0.8222 where the difference is less than 0.2. Thus, this model is significant and can be used for future predictions. It has been found that the interaction of factors BC has a major effect on the PE in comparison to other factors, due to the high F value of (18.33). The factor of AC interaction was found less contributing to PE.

The interactions between the variables in 3D response surface plots are shown in Figure 8(a)-(f). a indicated the combined effect of concentration (A) and duration (B) on PE at constant temperature (500 °C). The minimum PE of 82.98% was obtained. The combined effect of concentration (A) and temperature (C) on PE at constant duration (1 h) was shown in Figure 8(b), the minimum PE is 83.51% by the effect of concentration and time at a stable temperature. The combined effect of duration (B) and temperature (C) on PE at a constant concentration (50 ppm) was shown in Figure 8(c). The minimum PE is (82.43%) by the effect of concentration and time at a stable temperature. The contour plot in Figure 8(d)-(f) shows that when the temperature is fixed at 500 °C, the concentration and duration need to be maximized to achieve a low-rate constant. When concentration is kept at 50 ppm, temperature and duration need to be lowered to reduce the rate constant. These results agree with the optimised results of RC. When duration is kept at 1 h, concentration needs to be larger, but the temperature needs to be lower to have a lower rate constant.

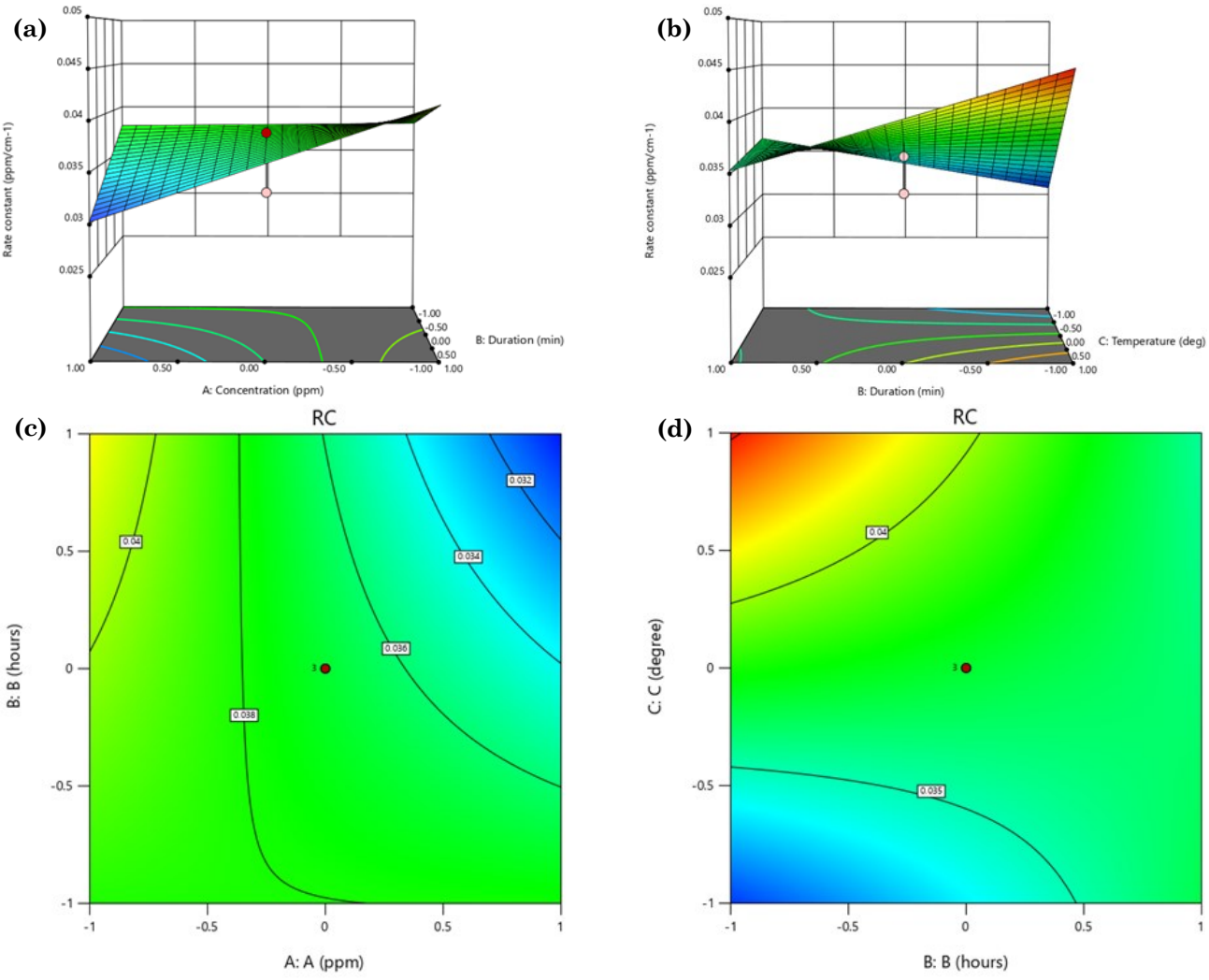

Figure 7. Combined effect of (a) concentration and duration at 500 °C annealing temperature (b) duration and temperature at 50 ppm Mn^{2+} ions concentration on RC. Contour plot of RC for (c) AB withhold value of temperature at 500 °C (d) BC withhold value of concentration at 50 ppm.

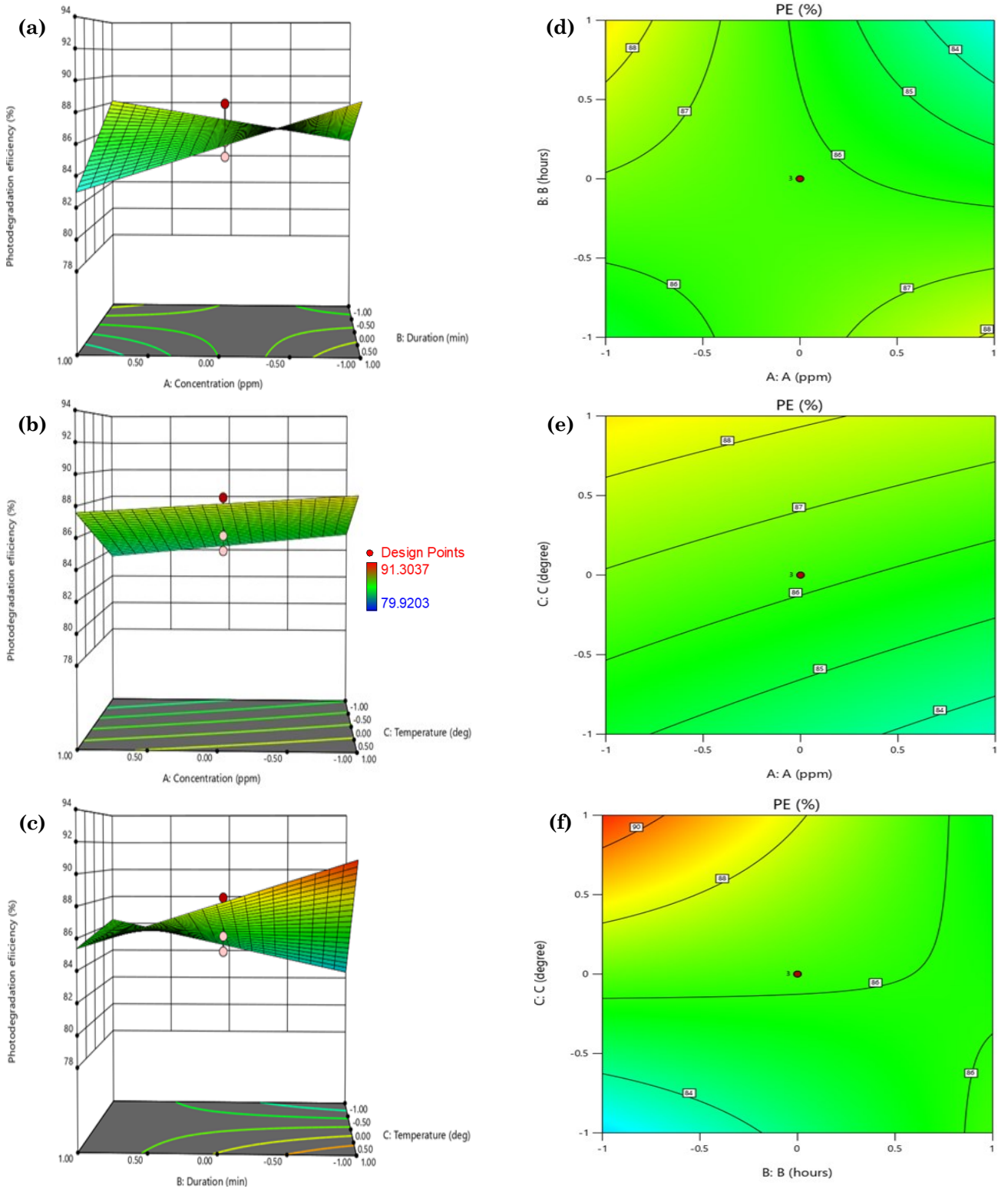

Figure 8. Combined effect of (a) concentration and duration at 500 °C annealing temperature, (b) concentration and temperature at 1 hour UV irradiation, (c) duration and temperature at 50 ppm Mn^{2+} ions concentration on PE, (d) AB with hold value of temperature at 500 °C, (e) AC with hold value of duration at 1 hour, and (f) BC withhold value of concentration at 50 ppm.

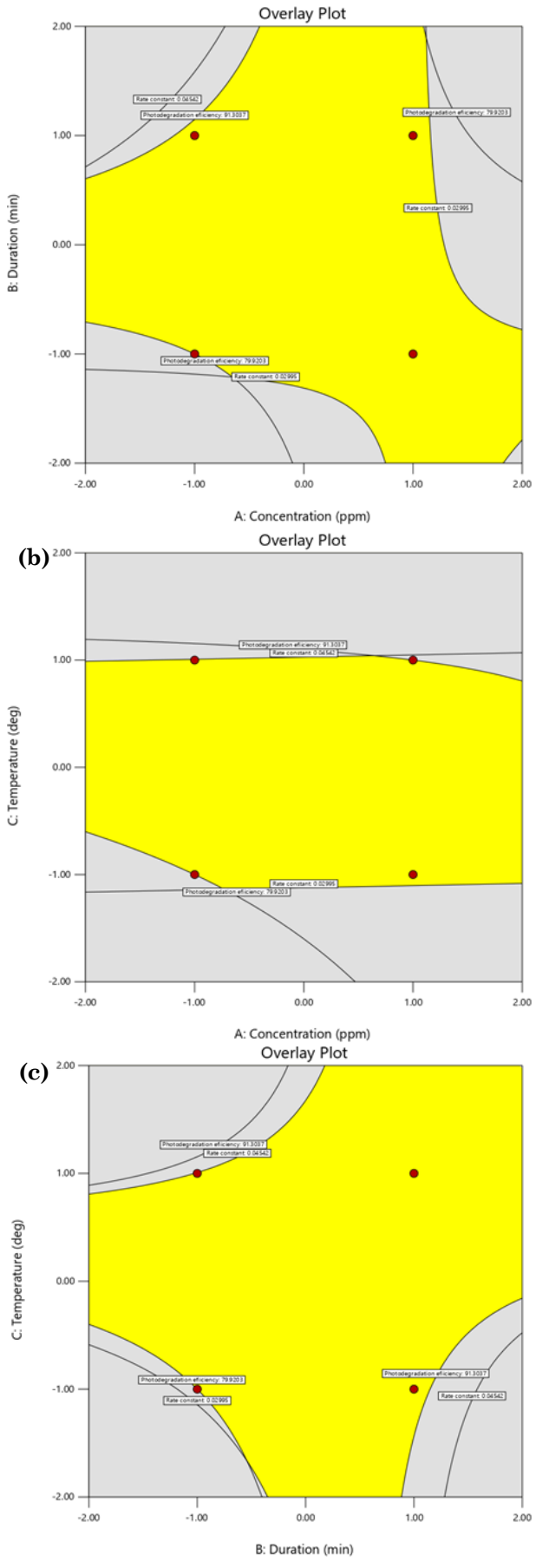

Figure 9. Overlay plot of RC and PE for (a) B versus A, (b) C versus A and (c) C versus B.

Final equation in terms of coded factors:

$$RC = 0.037 - 0.0029A - 0.001B + 0.0033C - 0.0028AB - 0.0039BC \quad (7)$$

$$PE = 86.24 - 0.6909A - 0.4067B + 1.89C - 2.16AB + 0.1482AC - 2.33BC + 1.21ABC \quad (8)$$

The combination solution for two responses (RC and PE) can be done using an overlay plot, as shown in Figure 9. The yellow-shaded region indicated the optimum result of RC and PE. The optimum synthesis parameters in this project to produce Mn-TiO_2 particles with low rate constant and photodegradation efficiency at 60 mins were 20 ppm of Mn^{2+} ion concentration that no significant terms and 200 ºC annealing temperature with UV irradiation. By using these parameters, the optimized photocatalytic performance (rate constant of 0.031 $ppm^{-1}.min^{-1}$ and 79.914% photodegradation efficiency at 60 min) can be achieved.

3.5. Characterization of Thin Film

From the conclusion made from Response Surface Methodology (RSM) optimization, Mn-TiO_2 (20 ppm Mn^{2+} ions, 200 °C annealing temperature) have the lowest rate constant (RC). In this work, particles were incorporated into epoxy resin and put under UV to test for their transmittance and refractive index (RI) perfor-

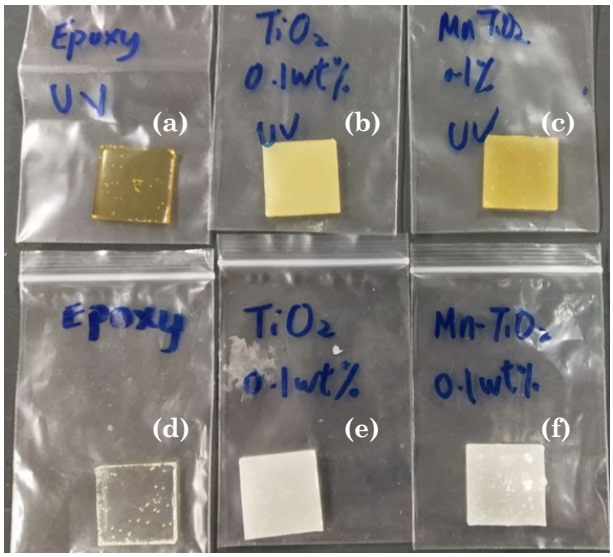

Figure 10. Thin film before UV irradiation for (a) epoxy resin, (b) epoxy resin incorporated with TiO_2 particles and (c) epoxy resin incorporated Mn-TiO_2 particles; thin film after UV irradiation for (d) epoxy resin, (e) epoxy resin incorporated with TiO_2 particles and (f) epoxy resin incorporated Mn-TiO_2 particles.

mances. The result shows that the RI of TiO_2 particles (2.391±0.005) is higher than Mn-TiO_2 particles (2.360±0.014), due to the crystallinity of TiO_2 particles being better than that of Mn-TiO_2 particles. As compared to the literature, the current strategy shows higher improvements in RI for Mn-TiO_2 particles. The slight reduction (1.3%) in RI was attributed to the Mn coupling. TiO_2 particles and Mn-TiO_2 particles were incorporated into epoxy resin and tested for the yellowing effect as shown in Figure 10.

Figure 11 shows the transmittance of pure epoxy resin compared to epoxy resin incorporated with TiO_2 particles and Mn-TiO_2 particles. Table 4 shows that the incorporation of Mn-TiO_2 particles inside a thin film of epoxy resin reduced the yellowing chromaticity effect and increased the RI. The transmittance of epoxy resin decreases when incorporated with particles. Nevertheless, the epoxy resin incorporated with Mn-TiO_2 particles has a higher transparency as compared to TiO_2 particles. This property is much needed in encapsulants as it could improve the light extraction efficacy of LEDs. Photodegradation of polymeric material depends on the exposure time and the intensity of radiation. The magnitude of this effect is typically dependent on the wavelength,

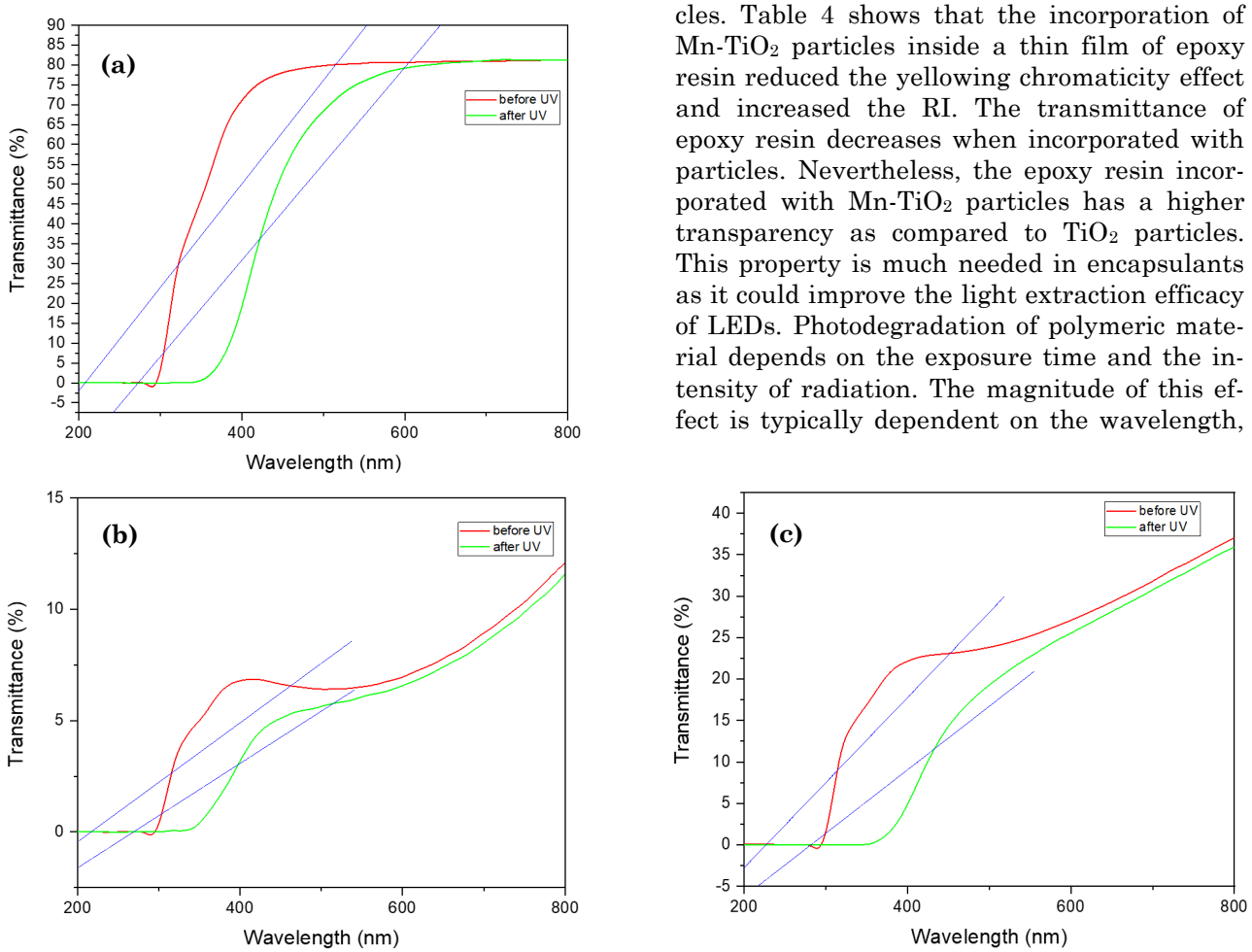

Figure 11. Transmittance measurement of (a) pure epoxy resin, (b) epoxy resin incorporated with TiO_2 particles, and (c) epoxy resin incorporated Mn-TiO_2 particles.

Table 4. Comparison of RI before and after UV of epoxy thin films.

No.	Epoxy			UV-Epoxy		
	Mn-TiO_2	TiO_2	Epoxy	UV-Mn-TiO_2	UV-TiO_2	UV Epoxy
1	2.173	2.386	1.914	2.070	2.285	2.154
2	2.172	2.386	1.904	2.055	2.275	2.151
3	2.169	2.395	1.909	2.060	2.288	2.150
4	2.176	2.368	1.909	2.063	2.271	2.150
5	2.170	2.374	1.907	2.064	2.285	2.153
6	2.178	2.368	1.905	2.068	2.275	2.150
7	2.167	2.391	1.910	2.059	2.280	2.151
8	2.169	2.391	1.907	2.048	2.251	2.152
9	2.168	2.425	1.910	2.047	2.274	2.151
10	2.177	2.383	1.909	2.059	2.300	2.153
Average	2.172	2.387	1.908	2.059	2.278	2.152
Std Dev.	0.004	0.017	0.003	0.008	0.013	0.001

with shorter wavelengths exhibiting larger attenuation [40]. The effect from high temperature of the LED chip causes the self-heating of the encapsulants which also contributes to the discolouration in the encapsulants [41]. Yazdan Mehr *et al*. reported the effect of both thermal and photooxidation that induced discolouration of BPA-PC. They have proven that the irradiation of UV accelerates the thermal yellowing of BPA-PC [9]. It is noted that the epoxy incorporated with Mn-TiO_2 shows a larger redshift of absorbance and transmittance after UV radiation compared to pure epoxy and epoxy-incorporated TiO_2. The blue line represented the gradient of the curve which corresponds to the changes in transmittance depending on wavelength. According to Abed & Turki Al-Rashid, when the energy gap increases, RI decreases and the transmittance increases [42,43]. The epoxy thin films after UV shows an increase in RI while epoxy incorporated with TiO_2 particles and Mn-TiO_2 particles shows a decrease in RI. Hendi *et al*. reported that the increment of RI was due to the presence of sub-oxidized material in the deposited film [44]. In addition, the reduction in RI is due to the decrease in the film density as photodegradation occurred [45].

4. Conclusions

Mn-TiO_2 particles were synthesised through photoreduction, confirmed by EDX and XRD analyses. The negatively charged surface of TiO_2 and Mn-TiO_2 particles indicated the potential for photodegradation. Mn-TiO_2 particles with 20 ppm Mn^{2+} and annealing at 200 °C showed improved dispersibility and minimal agglomeration. Mn-TiO_2 particles degrade MB with increasing UV time, showing 1st-order kinetics. Optimization was performed using Design of Experiment (DOE) and Response Surface Methodology (RSM) by modifying Mn^{2+} ion concentration, UV irradiation duration, and annealing temperature. The optimal synthesis parameters for Mn-TiO_2 particles with the lowest photocatalytic performance were determined as 20 ppm Mn^{2+} ions, 200 °C annealing temperature, and without UV irradiation. A redshift in transmittance in all epoxy-thin films was observed. The study showed that the incorporation of Mn-TiO_2 particles inside a thin film of epoxy resin reduced the yellowing effect and increased the refractive index (RI). The RI of epoxy resin incorporated with Mn-TiO_2 particles was lower than TiO_2 particles, but the transmittance was higher, which was helpful to achieve high light extraction efficacy in LED applications.

Acknowledgements

The authors gratefully acknowledge the financial support of the Ministry Of Higher Education Malaysia For the Fundamental Research Grant Scheme With Project Code: FRGS/1/2022/STG05/USM/03/3 and the support from the Universiti Sains Malaysia.

CRediT Author Statement

Author Contributions: Amna Jwad Kadem: Conceptualization, Data curation, Formal analysis, Investigation, Methodology, Roles/Writing - original draft. Teo Yin Xin: Conceptualization, Data curation, Formal analysis, Investigation, Methodology, Roles/Writing - original draft. Swee-Yong Pung: Conceptualization, Formal analysis, Funding acquisition, Resources, Validation, Writing - review & editing. Srimala Sreekantan: Conceptualization, Formal analysis, Funding acquisition, Resources, Validation, Writing - review & editing. Ramakrishnan Sivakumar: Conceptualization, Formal analysis, Investigation, Project administration, Resources, Supervision, Validation, Writing - review & editing. All authors have read and agreed to the published version of the manuscript.

References

[1] Parbrook, P.J., Corbett, B., Han, J., Seong, T.Y., Amano, H. (2021). Micro-Light Emitting Diode: From Chips to Applications. *Laser and Photonics Reviews*, 15(5), 2000133. DOI: 10.1002/lpor.202000133.

[2] Holonyak, N., Bevacqua, S.F. (1962). Coherent (visible) light emission from Ga(As1-xPx) junctions. *Applied Physics Letters*, 1(4), 82–83. DOI: 10.1063/1.1753706.

[3] Manikandan, M., Nirmal, D., Ajayan, J., Mohankumar, P., Prajoon, P., Arivazhagan, L. (2019). A review of blue light emitting diodes for future solid state lighting and visible light communication applications. *Superlattices and Microstructures*, 136, 106294. DOI: 10.1016/j.spmi.2019.106294.

[4] Peng, Z., Lu, Y., Gao, Y., Chen, G., Zheng, J., Guo, Z., Lin, Y., Chen, Z. (2018). Effect of carrier localization and shockley-read-hall recombination on the spatial distribution of electroluminescence in InGaN LEDs. *IEEE Photonics Journal*, 10(6), 8201908. DOI: 10.1109/JPHOT.2018.2880319.

[5] Wang, C.H., Chen, J.R., Chiu, C.H., Kuo, H.C., Li, Y.-L., Lu, T.C., Wang, S.C., (2010). Temperature-dependent electroluminescence efficiency in blue InGaN-GaN light-emitting diodes with different well widths. *IEEE Photonics Technology Letters*, 22(4), 236–238. DOI: 10.1109/LPT.2009.2037827.

[6] Yan, M.M., Li, Y., Zhou, Y.-T., Liu. L., Zhang, Y., You, B.-G., Li, Y. (2017). Enhancing the Performance of Blue Quantum-Dot Light-Emitting Diodes Based on Mg-Doped ZnO as an Electron Transport Layer. *IEEE Photonics Journal*, 9(2), 8200508. DOI: 10.1109/JPHOT.2017.2666423.

[7] Huang, P., Shi, H.Q., Xiao, H.M., Li, Y.Q., Hu, N., Fu, S.Y. (2017). High performance surface-modified TiO_2/silicone nanocomposite. *Scientific Reports*, 7(1), 5951. DOI: 10.1038/s41598-017-05166-7.

[8] Kim, A.Y., Götz, W., Steigerwald, D.A., Wierer, J.J., Gardner, N.F., Sun, J., Stockman, S.A., Martin, P.S., Krames, M.R., Kern, R.S., Steranka, F.M. (2001). Performance of High-Power AlInGaN Light Emitting Diodes. *Physica Status Solidi (A) – Applications and Materials Science*, 188(1), 15–21. DOI: 10.1002/1521-396X(200111)188:1<15::AID-PSSA15>3.0.CO;2-5.

[9] Yazdan Mehr, M., Bahrami, A., van Driel, W.D., Fan, X.J., Davis, J.L., Zhang, G.Q. (2020). Degradation of optical materials in solid-state lighting systems. *International Materials Reviews*, 65(2), 102–128. DOI: 10.1080/09506608.2019.1565716.

[10] Lu, Q., Yang, Z., Meng, X., Yue, Y., Ahmad, M.A., Zhang, W., Zhang, S., Zhang, Y., Liu, Z., Chen, W. (2021). A Review on Encapsulation Technology from Organic Light Emitting Diodes to Organic and Perovskite Solar Cells. *Advanced Functional Materials*, 31(23), 2100151. DOI: 10.1002/adfm.202100151.

[11] Kim, J.S., Yang, S., Bae, B.S. (2010). Thermally stable transparent sol-gel based siloxane hybrid material with high refractive index for light emitting diode (LED) encapsulation. *Chemistry of Materials*, 22(11), 3549–3555. DOI: 10.1021/cm100903b.

[12] Fan, J., Chen, Y., Jing, Z., Ibrahim, M.S., Cai, M. (2021). A Gamma process-based degradation testing of silicone encapsulant used in LED packaging. *Polymer Testing*, 96, 107090. DOI: 10.1016/j.polymertesting.2021.107090.

[13] Huang, J.H., Li, C.P., Chang-Jian, C.W., Lee, K.C., Huang, J.H. (2015). Preparation and characterization of high refractive index silicone/TiO_2 nanocomposites for LED encapsulants. *Journal of the Taiwan Institute of Chemical Engineers*, 46, 168–175. DOI: 10.1016/j.jtice.2014.09.008.

[14] Huang, Y., Feng, Y., Sun, X., Han, Y., Liu, D., Tan, X. (2019). Preparation of ZrO_2/silicone hybrid materials for LED encapsulation via in situ sol-gel reaction. *Polymers for Advanced Technologies*, 30(7), 1818–1824. DOI: 10.1002/pat.4614.

[15] Dan, S., Gu, H., Tan, J., Zhang, B., Zhang, Q. (2018). Transparent epoxy/TiO_2 optical hybrid films with tunable refractive index prepared via a simple and efficient way. *Progress in Organic Coatings*, 120, 252–259. DOI: 10.1016/j.porgcoat.2018.02.017.

[16] Huang, J.C., Chu, Y.P., Wei, M., Deanin, R.D. (2004). Comparison of epoxy resins for applications in light-emitting diodes. *Advances in Polymer Technology*, 23(4), 298–306. DOI: 10.1002/adv.20018.

[17] Huang, K.C., Huang, Y.R., Chuang, T.L., Ting, S.Y., Tseng, S.H., Huang, J.E. (2015). Incorporation of anatase TiO_2 particles into silicone encapsulant for high-performance white LED. *Materials Letters*, 143, 244–247. DOI: 10.1016/j.matlet.2014.12.134.

[18] Wang, P.C., Lin, C.L., Su, Y.K., Chien, P.C., Huang, G.S., Kuo, S.C., Lyu, G.C. (2014). Effects of TiO2-doped silicone encapsulation material on the light extraction efficiency of GaN-based blue light-emitting diodes. *Thin Solid Films*, 570, 273–276. DOI: 10.1016/j.tsf.2014.05.021.

[19] Grassie, N., Guy, M.I., Tennent, N.H. (1985). Degradation of epoxy polymers: Part 1—Products of thermal degradation of bisphenol-A diglycidyl ether. *Polymer Degradation and Stability*, 12(1), 65–91. DOI: 10.1016/0141-3910(85)90057-6.

[20] Jain, P., Choudhary, V., Varma, I.K. (2003). Effect of structure on thermal behaviour of epoxy resins. *European Polymer Journal*, 39(1), 181–187. DOI: 10.1016/S0014-3057(02)00191-X.

[21] Wang, X., Hu, Y., Song, L., Xing, W., Lu, H., Lv, P., Jie, G. (2010). Flame retardancy and thermal degradation mechanism of epoxy resin composites based on a DOPO substituted organophosphorus oligomer. *Polymer*, 51(11), 2435–2445. DOI: 10.1016/j.polymer.2010.03.053.

[22] Chung, Y.T., Ba-Abbad, M.M., Mohammad, A.W., Benamor, A. (2016). Functionalization of zinc oxide (ZnO) nanoparticles and its effects on polysulfone-ZnO membranes. *Desalination and Water Treatment*, 57(17), 7801–7811. DOI: 10.1080/19443994.2015.1067168.

[23] Alkallas, F.H., Elshokrofy, K.M., Mansour, S.A. (2019). Structural and diffuse reflectance characterization of cobalt-doped titanium dioxide nanostructured powder prepared via facile sonochemical hydrolysis technique. *Nanomaterials and Nanotechnology*, 9, 1-7. DOI: 10.1177/1847980419847806.

[24] Mont, F.W., Kim, J.K., Schubert, M.F., Schubert, E.F., Siegel, R.W. (2008). High-refractive-index TiO_2-nanoparticle-loaded encapsulants for light-emitting diodes. *Journal of Applied Physics,* 103, 083120. DOI: 10.1063/1.2903484.

[25] Humayun, M., Raziq, F., Khan, A., Luo, W. (2018). Modification strategies of TiO_2 for potential applications in photocatalysis: A critical review. *Green Chemistry Letters and Reviews*, 11(2), 86–102. DOI: 10.1080/17518253.2018.1440324.

[26] Le, A.T., Tan, Z.H., Sivakumar, R., Pung, S.Y. (2021). Predicting the photocatalytic performance of metal/metal oxide coupled TiO_2 particles using Response Surface Methodology (RSM). *Materials Chemistry and Physics*, 269, 124739. DOI: 10.1016/j.matchemphys.2021.124739.

[27] Pinton, A.P., Bulhões, L.O.D.S. (2019). Synthesis, characterization, and photostability of manganese-doped titanium dioxide nanoparticles and the effect of manganese content. *Materials Research Express*, 6(12), 125015. DOI: 10.1088/2053-1591/ab533b.

[28] Sakkas, V.A., Islam, M.A., Stalikas, C., Albanis, T.A. (2010). Photocatalytic degradation using design of experiments: A review and example of the Congo red degradation. *Journal of Hazardous Materials*, 175(1–3), 33–44. DOI: 10.1016/j.jhazmat.2009.10.050.

[29] Rajkumar, K., Muthukumar, M. (2017). Response surface optimization of electro-oxidation process for the treatment of C.I. Reactive Yellow 186 dye: reaction pathways. *Applied Water Science*, 7(2), 637–652. DOI: 10.1007/s13201-015-0276-0.

[30] Song, C., Li, X., Wang, L., Shi, W. (2016). Fabrication, Characterization and Response Surface Method (RSM) Optimization for Tetracycline Photodegration by $Bi_{3.84}W_{0.16}O_{6.24}$-graphene oxide (BWO-GO). *Scientific Reports*, 6, 37466. DOI: 10.1038/srep37466.

[31] Babaei, A.A., Mesdaghiniai, A.R., Haghighi, N.J., Nabizadeh, R., Mahvi, A.H. (2011). Modeling of nonylphenol degradation by photo-nanocatalytic process via multivariate approach. *Journal of Hazardous Materials*, 185(2–3), 1273–1279. DOI: 10.1016/j.jhazmat.2010.10.042.

[32] Cody, D., Babeva, T., Madjarova, V., Kharchenko, A., Gul, S.E., Mintova, S., Barrett, C.J., Naydenova, I. (2020). In-situ ellipsometric study of the optical properties of LTL-doped thin film sensors for copper(II) ion detection. *Coatings*, 10(4), 423. DOI: 10.3390/coatings10040423.

[33] Phromma, S., Wutikhun, T., Kasamechonchung, P., Eksangsri, T., Sapcharoenkun, C. (2020). Effect of calcination temperature on photocatalytic activity of synthesized TiO2 nanoparticles via wet ball milling sol-gel method. *Applied Sciences*, 10(3), 993. DOI: 10.3390/app10030993.

[34] Díaz-Uribe, C., Viloria, J., Cervantes, L., Vallejo, W., Navarro, K., Romero, E., Quiñones, C. (2018). Photocatalytic activity of Ag-TiO2 composites deposited by photoreduction under UV irradiation. *International Journal of Photoenergy*, 2018, 6080432. DOI: 10.1155/2018/6080432.

[35] Hannula, M., Ali-Löytty, H., Lahtonen, K., Sarlin, E., Saari, J., Valden, M. (2018). Improved Stability of Atomic Layer Deposited Amorphous TiO_2 Photoelectrode Coatings by Thermally Induced Oxygen Defects. *Chemistry of Materials*, 30(4), 1199–1208. DOI: 10.1021/acs.chemmater.7b02938.

[36] Ermrich, M., Opper, D. (2013). *XRD for the Analyst: Getting Acquainted with the Principles*. PANalytical.

[37] Lau, Y.Y., Wong, Y.S., Teng, T.T., Morad, N., Rafatullah, M., Ong, S.A. (2015). Degradation of cationic and anionic dyes in coagulation-flocculation process using bi-functionalized silica hybrid with aluminum-ferric as auxiliary agent. *RSC Advances*, 5(43), 34206–34215. DOI: 10.1039/c5ra01346a.

[38] Joseph, C.G., Elilarasi, L. (2017). Removal of Methylene Blue Dye from Aqueous Solution Using a Newly Synthesized TiO_2-SiO_2 Photocatalyst in the Presence of Active Chlorine Species. *IOP Conference Series: Materials Science and Engineering*, 206, 012090. DOI: 10.1088/1757-899X/206/1/012090.

[39] Wang, C., Yao, J. (2010). Decolorization of methylene blue with TiO_2 sol via UV irradiation photocatalytic degradation. *International Journal of Photoenergy*, 2010, 643182. DOI: 10.1155/2010/643182.

[40] Davis, J.L., Mills, K., Lamvik, M., Solano, E., Bobashev, G., Perkins, C. (2017). Modeling the Impact of Thermal Effects on Luminous Flux Maintenance for SSL Luminaires. *2017 16th IEEE Intersociety Conference on Thermal and Thermomechanical Phenomena in Electronic Systems (ITherm)*, 2017, 1004-1010. DOI: 10.1109/ITHERM.2017.7992598.

[41] Meneghesso, G., Meneghini, M., Zanoni, E. (2010). Recent results on the degradation of white LEDs for lighting. *Journal of Physics D: Applied Physics*, 43(35), 354007. DOI: 10.1088/0022-3727/43/35/354007.

[42] Hervé, P.J.L., Vandamme, L.K.J. (1995). Empirical temperature dependence of the refractive index of semiconductors. *Journal of Applied Physics*, 77, 5476–5477. DOI: 10.1063/1.359248.

[43] Abed, S.M., Turki Al-Rashid, S.N. (2018). Study of the effects of nano-particle sizes on the transmittance of CdTe thin film. *Chalcogenide Letters*, 15(5), 237–246.

[44] Hendi, A.H.Y., Al-Kuhaili, M.F., Durrani, S.M.A. (2016). Chemical and optical properties of MnO_2 thin films prepared by reactive evaporation of manganese. *International Journal of Research in Engineering and Technology*, 5, 320–328. DOI: 10.15623/IJRET.2016.0505059.

[45] Mohamed, S.H., Mohamed, H.A., Abd El Ghani, H.A. (2011). Development of structural and optical properties of WOx films upon increasing oxygen partial pressure during reactive sputtering. *Physica B Condens. Matter.*, 406(4), 831–835. DOI: 10.1016/j.physb.2010.12.005.

Supplementary Materials

Table S1. ANOVA results for RC.

Source	Sum of Squares	df	Mean Square	F-value	p-value	
Model	0.0003	7	0.0000	4.83	0.1820	not significant
A-A	0.0001	1	0.0001	6.53	0.1250	
B-B	8.736E-06	1	8.736E-06	0.8498	0.4539	
C-C	0.0001	1	0.0001	8.51	0.1001	
AB	0.0001	1	0.0001	5.90	0.1359	
AC	1.445E-06	1	1.445E-06	0.1406	0.7438	
BC	0.0001	1	0.0001	11.73	0.0757	
ABC	1.882E-06	1	1.882E-06	0.1830	0.7104	
Curvature	8.015E-06	1	8.015E-06	0.7796	0.4704	
Pure Error	0.0000	2	0.0000			
Cor Total	0.0004	10				
Std. Dev.	0.0032	R^2	0.9442			
Mean	0.0365	Adjusted R^2	0.7489			
C.V. %	8.79	Predicted R^2	NA(1)			
		Adeq Precision	5.3340			

Table S2. ANOVA results for RC after optimization using RSM.

Source	Sum of Squares	df	Mean Square	F-value	p-value	
Model	0.0003	5	0.0001	11.54	0.0172	significant
A-A	0.0001	1	0.0001	11.25	0.0285	
B-B	8.736E-06	1	8.736E-06	1.46	0.2931	
C-C	0.0001	1	0.0001	14.65	0.0186	
AB	0.0001	1	0.0001	10.15	0.0334	
BC	0.0001	1	0.0001	20.19	0.0109	
Curvature	8.015E-06	1	8.015E-06	1.34	0.3111	
Residual	0.0000	4	5.972E-06			
Lack of Fit	3.327E-06	2	1.663E-06	0.1618	0.8607	not significant
Pure Error	0.0000	2	0.0000			
Cor Total	0.0004	10				
Std. Dev.	0.0024	R^2	0.9352			
Mean	0.0365	Adjusted R^2	0.8541			
C.V. %	6.70	Predicted R^2	0.7300			
		Adeq Precision	8.0278			

Table S3. ANOVA results for PE.

Source	Sum of Squares	df	Mean Square	F-value	p-value	
Model	126.46	7	18.07	5.08	0.1742	not significant
A-A	3.82	1	3.82	1.07	0.4088	
B-B	1.32	1	1.32	0.3724	0.6038	
C-C	28.53	1	28.53	8.03	0.1053	
AB	37.36	1	37.36	10.51	0.0834	
AC	0.1756	1	0.1756	0.0494	0.8447	
BC	43.55	1	43.55	12.26	0.0728	
ABC	11.70	1	11.70	3.29	0.2112	
Curvature	0.0208	1	0.0208	0.0059	0.9460	
Pure Error	7.11	2	3.55			
Cor Total	133.59	10				
Std. Dev.	1.89	R^2	0.9468			
Mean	86.24	Adjusted R^2	0.7606			
C.V. %	2.19	Predicted R^2	NA(1)			
		Adeq Precision	6.6763			

Table S4. ANOVA results for PE after optimization using RSM.

Source	Sum of Squares	df	Mean Square	F-value	p-value	
Model	126.46	7	18.07	7.60	0.0617	not significant
A-A	3.82	1	3.82	1.61	0.2943	
B-B	1.32	1	1.32	0.5570	0.5096	
C-C	28.53	1	28.53	12.01	0.0405	
AB	37.36	1	37.36	15.73	0.0286	
AC	0.1756	1	0.1756	0.0739	0.8033	
BC	43.55	1	43.55	18.33	0.0234	
ABC	11.70	1	11.70	4.93	0.1131	
Residual	7.13	3	2.38			
Lack of Fit	0.0208	1	0.0208	0.0059	0.9460	not significant
Pure Error	7.11	2	3.55			
Cor Total	133.59	10				
Std. Dev.	1.54	R^2	0.9466			
Mean	86.24	Adjusted R^2	0.8222			
C.V. %	1.79	Predicted R^2	0.8990			
		Adeq Precision	8.6601			